

Vibration Reduction and Torque Improvement of Integral-slot SPM Machines Using PM Harmonic Injection*

Jinghua Ji, Deyou Liu, Yu Zeng, Tong Liu and Wenxiang Zhao*

(School of Electrical and Information Engineering, Jiangsu University, Zhenjiang 212013, China)

Abstract: This study aimed to improve the vibration and torque of an integral-slot surface-mounted permanent magnet (SPM) machine by optimizing the shape of the harmonically injected permanent magnet (PM). First, the effect of the third harmonic injected into the sinusoidal PM shape on the electromagnetic performance of a 36-slot/12-pole SPM machine was investigated, including the torque performance and vibration response. It was found that the Sin+3rd harmonic-shaped PM had a contrary effect on the torque and vibration performance of the integral-slot machine, which improved the torque capability but worsened the vibration performance. Second, the response surface model and Barebones multi-objective particle swarm optimization algorithm based on a trade-off between the average torque and vibration were implemented to determine the optimal harmonic injection. Subsequently, the performances of the optimal Sin+3rd-shaped and eccentric PM machines were compared, showing the excellent torque and vibration performance of the adopted method. Finally, a prototype was manufactured and tested to verify the results of the theoretical analysis.

Keywords: Integral-slot, surface-mounted permanent magnet machine, multi-objective optimization, third harmonic, torque, vibration

1 Introduction

Owing to their high efficiency and power density, integral-slot surface-mounted permanent magnet (SPM) machines have been widely applied in areas such as servo drives and electricity propulsion [1-3]. High torque performance and low vibration are required for integral-slot SPM machines to meet the growing need for high performance [4-6]. However, a mutual restriction exists between high torque density and low vibration [7-9]. Therefore, it is important to investigate an integral-slot SPM machine with a high torque performance and low vibration response.

Traditionally, eccentric permanent magnets (PM) have been identified as an attractive approach for reducing the torque ripple and electromagnetic vibration in machines. An eccentric PM was designed to reduce torque ripple [10-11], and the torque ripple and

vibration performance were simultaneously improved [12]. Low- and medium-frequency vibrations were reduced using eccentric PMs and dummy slots [13]. However, most of the above studies were based on torque ripple and vibration reduction, resulting in an unacceptable drop in torque capability.

Numerous approaches have been proposed to improve the torque performance, among which PM shaping with harmonic injection is an effective method. Theoretical derivation and finite element analysis (FEA) indicate that an appropriate value of the third harmonic injected into the PM shape can increase the average torque while maintaining a low torque ripple [14-15]. However, the optimal value of injected harmonics is unknown. A PM shape based on a feedback function was proposed to obtain a superior harmonic-injected amplitude, further improving the torque capability [16]. In addition, the differences between various harmonic injection methods were explored, confirming the advantages of high-torque performance [17]. The harmonic amplitude injected into a PM was adjusted using multi-objective optimization to obtain a higher average torque [18]. The above studies indicate that a third-harmonic injected PM

Manuscript received January 13, 2023; revised February 23, 2023; accepted March 11, 2023. Date of publication December 31, 2023; date of current version August 23, 2023.

* Corresponding Author, E-mail: zwx@ujs.edu.cn

* Supported by National Natural Science Foundation of China (52025073).

Digital Object Identifier: 10.23919/CJEE.2023.000028

could enhance torque capability. However, the electromagnetic vibration performance was neglected.

For integral-slot machines, zeroth-order vibrations have been found to be significant^[19]. The zeroth-order electromagnetic force is the primary vibration source^[20]. In Ref. [21], it was revealed that higher-order radial forces can generate lower-order radial forces and zeroth-order vibrations under a modulation effect. Moreover, the vibration was significant for the zeroth-order electromagnetic force at the slot number frequency^[22]. The vibration response was investigated for various orders of radial forces at slot number frequencies^[23], which revealed that the slot-number-order radial force was the main vibration source. In addition, a teeth-chopping effect was proposed and explained theoretically. The slot number order radial force for an integral-slot PM machine was optimized to improve the vibration performance^[24]. However, most of the above studies were biased toward vibration reduction, resulting in an unacceptable drop in torque capability. Furthermore, the vibration of the integral-slot machine was adversely affected by the third harmonic of the PM magnetic field^[12]. Considering the mutually conflicting effect that the third harmonic exerts on the torque and vibration, multi-objective optimization was employed to avoid conflicts among the parameters. Furthermore, a substitute model with reliable accuracy is essential for improving the optimization efficiency, particularly for machines with various optimized parameters. Response surface models (RSM) have been widely employed to establish alternative models and improve optimization efficiency^[25-27].

This study aims to improve the vibration and torque performance of an integral-slot SPM machine by adjusting the harmonic-injected PM shape, resulting in low vibration and high torque performance. The optimization goal includes several elements such as the average torque, torque ripple, and radial force. A multi-objective optimization method integrating the RSM and Barebones multi-objective particle swarm optimization (BB-MOPSO) algorithm was employed to enhance the global search capability and convergence rate. The remainder of this paper is organized as follows. In Section 2, the effects of the third harmonic injected into the sinusoidal PM shape

on the vibration and torque performance of an integral-slot SPM machine are discussed. In Section 3, the RSM and BB-MOPSO algorithm are employed to optimize the harmonic-injected PM shape, and the superiority of the optimal machine is verified. In Section 4, a prototype is developed to verify the proposed method. Finally, the conclusions are presented in Section 5.

2 PM shape and performance analysis

2.1 Initial and eccentric PM machines

The electromagnetic performance of the 36-slot/12-pole integral-slot SPM machine, including the air-gap magnetic flux density, average torque, and torque ripple, is examined in this section. The geometry of the machine and its flux distribution at the rated load are illustrated in Fig. 1. The primary parameters are listed in Tab. 1. Fig. 2 shows the structure of an eccentric PM, where R_1 and R_2 are the circular radii of the initial and eccentric PM, respectively. O is the circle center of the initial PM, O_1 is the external radius circle center of the PM when it is eccentric, h is the eccentric distance, and h_{\max} is the maximum thickness of the PM.

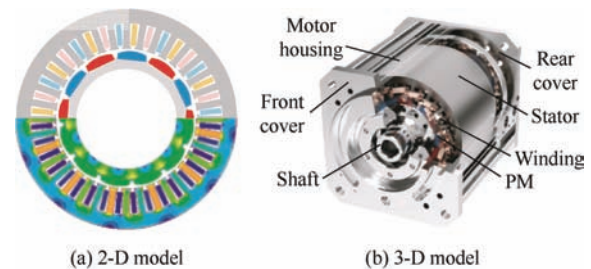


Fig. 1 Geometry and flux distribution of 36-slot/12-pole SPM machine

Tab. 1 Main specifications of 36-slot/12-pole SPM machine

Parameter	Value
Stator slot/rotor pole	36/12
Rated speed/(r/min)	1 000
Rated power/kW	3
Rate current/A	6.3
Rate voltage/V	215
Rate torque/(N · m)	11.7
Stack length/mm	90
Stator outer diameter/mm	125
Stator inner diameter/mm	80
Eccentric distance/mm	20
Air-gap length/mm	1.5
Turn number per coil	36

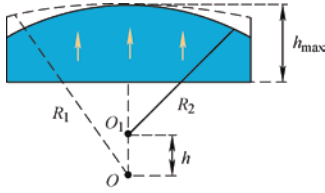


Fig. 2 Eccentric PM structure

Generally, an eccentric PM can effectively reduce the torque ripple. Fig. 3a shows the variation in torque performance with the eccentric distance. An eccentric distance of 20 mm exhibited a lower torque ripple than other distances when achieving the rated torque. Fig. 3b shows the variation in the amplitude of the p^{th} - and $3p^{\text{th}}$ -order air-gap radial magnetic flux density harmonic components with the eccentricity distance. The amplitudes of the p^{th} - and $3p^{\text{th}}$ -order components degraded with an increase in the eccentric distance. When the eccentric distance exceeded 20 mm, the $3p^{\text{th}}$ -order components degraded, but the torque ripple suppressed slowly, even deteriorated after the eccentric distance of 22 mm. However, the average torque decreased significantly. Therefore, considering torque performance, the eccentric distance of the PM was selected as 20 mm. Fig. 4 compares the air-gap radial magnetic flux density and harmonic content of the machines with those of the initial and eccentric PM. The eccentric PM machine presented a more sinusoidal waveform than the initial PM machine, derived from its lower harmonic content.

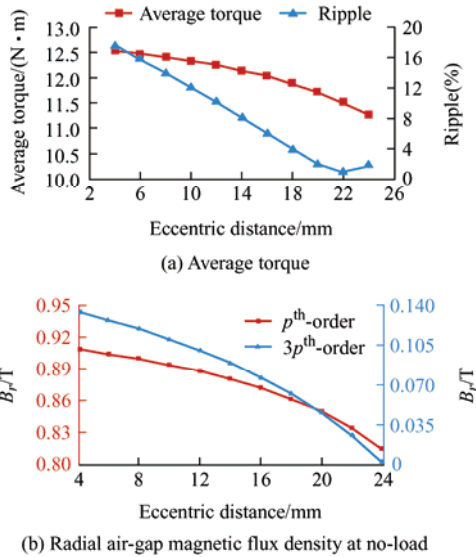


Fig. 3 Varying machine performance based on eccentric distance of PM

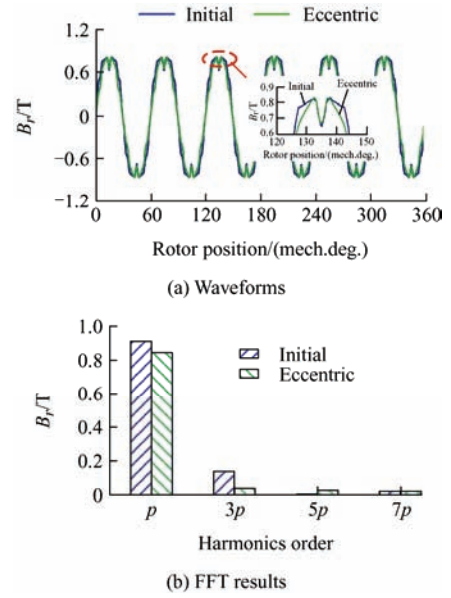


Fig. 4 Radial air-gap magnetic flux density at no-load for initial and eccentric PM machines

Fig. 5 shows the torque performance of both machines at a rated load of 1 000 r/min. The eccentric PM machine exhibited a low torque ripple, which is attributed to its reduced harmonic content. However, the fundamental amplitude diminished excessively, which reduced the average torque.

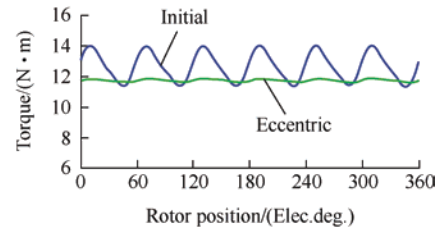


Fig. 5 Torque performance of machines with initial and eccentric PM

A PM shaping with harmonic injection was adopted in this study to improve the torque performance of the machine. Details of this process are described in the following subsections.

2.2 Harmonic injected PM shape

Sine shaping with a third harmonic injected into the PM improves torque performance [14-15]. To further strengthen the optimal harmonic amplitude, a PM shape based on a feedback function proposed in Ref. [16] was adopted, as shown in Fig. 6. The feedback function $h_{m2}(\theta)$ can be described as

$$\begin{cases} h_{m2}(\theta) = h_{m1}(\theta) + h_{\max} - \Delta m - [B'_1(\theta) - B'_2(\theta)] \frac{l}{B_{rm}} \mu \\ \Delta m = h_{\max} - [(B'_1(\theta) - B'_2(\theta)) l \mu / B_{rm}]_{\min} \end{cases} \quad (1)$$

where $h_{m1}(\theta)$ is the thickness function of the initial PM, and its maximum value is h_{max} ; $B'_1(\theta)$ is the actual air-gap flux density function; $B'_2(\theta)$ is the objective function in the optimization field; B_{rm} is the remanence of the PM; l is the total length of the PM and air gap; Δm is intended to maintain the minimum air-gap length δ_{air} as constant; and μ is an adjustment parameter to compensate for the slot effect.

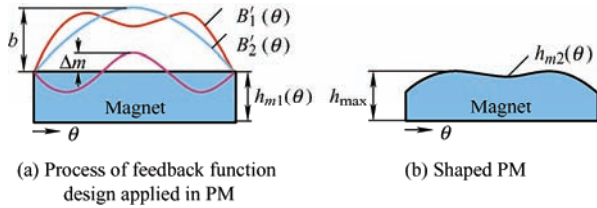


Fig. 6 Feedback function design applied to PM

By integrating Eq. (1) and the simulation, the amplitudes of the fundamental and adjustment coefficients were 1.8 and 0.3, respectively, achieving superior torque performance. However, the average torque loss was severe at 10.8 N · m. The third harmonic was injected into the PM to improve the average torque, and the torque performance variation with b_3 is shown in Fig. 7. When the amplitude of the third harmonic reached 0.3, the average torque was maximized while maintaining a low torque ripple; therefore, it was selected as 0.3. The torque ripple remained in space for optimization, despite that the average torque was increased to 12.4 N · m.

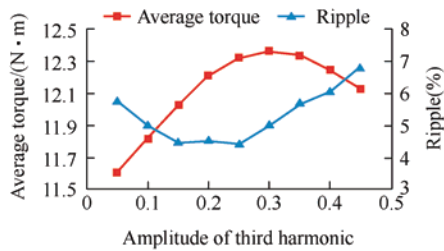


Fig. 7 Torque performance based on the amplitude of the third harmonic

The selection process for these parameters was affected by subjective factors. Therefore, PM shaping with sine and third-harmonic injections (Sin+3rd-shaped PM machine) was carried out simultaneously in this study. The objective function can be expressed as

$$B'_2(\theta) = b_1 \sin(p\theta) + b_3 \sin(3p\theta) \quad (2)$$

For further accuracy, the variation ranges of the

fundamental harmonic, third harmonic, and compensation coefficients were limited to approximately those of the above single-parameter optimal values. Function $\Delta m(b_1, b_3, \mu)$ was derived by discretization and fitting, as expressed in Eq. (3). Their comprehensive optimal values were selected using a multiobjective algorithm, as introduced in Section 3, as follows

$$\begin{aligned} \Delta m = & 5.74 - 0.69b_1 - 10.35b_3 - 3.38\mu + 8.80b_1b_3 + 3.49b_1\mu - \\ & 1.99b_3\mu + 0.27b_1^2 + 32.08b_3^2 - 0.016\mu^2 - 6.64b_1b_3\mu + \\ & 0.63b_3b_1^2 + 1.55\mu b_1^2 - 45.51b_1b_3^2 + 23.84\mu b_3^2 + \\ & 0.0037b_1\mu^2 - 0.002b_3\mu^2 - 0.18b_1^3 + 31.54b_3^3 - \\ & 0.21\mu b_1^3 + 56.61b_1b_3^3 - 0.48\mu b_3^3 - 0.004b_1\mu^3 + \\ & 0.029\mu^3 + 0.043b_3b_1^3 + 0.002b_3\mu^3 + \\ & 0.025b_1^4 - 127.78b_3^4 - 0.02\mu^4 \end{aligned} \quad (3)$$

However, the effect of PM shaping with harmonic injection on the vibration performance of machines has not yet been investigated in previous studies. Therefore, this study investigated the comprehensive effect of the Sin+3rd-shaped PM machine on torque and vibration performance.

2.3 Radial force and vibration

As the tangential flux density is much smaller than the radial flux density, the tangential component is neglected when calculating the radial force. According to the Maxwell tensor method, the radial force density can be expressed as ^[28-29]

$$f_r(\theta, t) \approx \frac{B_r^2}{2\mu_0} = \frac{1}{2\mu_0} (B_{PM}^2 + B_{ARM}^2 + 2B_{PM}B_{ARM}) \quad (4)$$

where B_r is the radial air-gap magnetic flux density, B_{PM} is the PM field air-gap magnetic flux density, B_{ARM} is the armature field air-gap magnetic flux density, and μ_0 is the vacuum permeability.

Tab. 2 lists the spatial order and frequency of the radial force harmonics generated by the PM magnetic field self-interaction and the armature field interaction with the PM magnetic field. In Tab. 2, Q is the number of stator slots, p is the number of rotor poles, F_m is the amplitude of the m^{th} -order PM magnetomotive force, F_v is the amplitude of the v^{th} -order armature magnetomotive force, A_0 is the DC component of the

air-gap permeance, and A_k is the v^{th} -order air-gap permeance.

Tab. 2 Radial force harmonics distribution

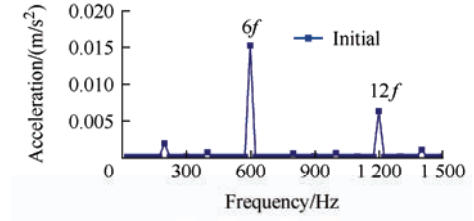
Source	Order	Frequency	Amplitude
	$(m_1 \pm m_2)p$	$(m_1 \pm m_2)f$	$A_0^2 F_{m_1} F_{m_2} / 4\mu_0$
PM	$(m_1 \pm m_2)p \pm kQ$	$(m_1 \pm m_2)f$	$A_0 A_k F_{m_1} F_{m_2} / 4\mu_0$
	$(m_1 \pm m_2)p \pm 2kQ$	$(m_1 \pm m_2)f$	$A_{k1} A_{k2} F_{m_1} F_{m_2} / 16\mu_0$
PM & armature	$(m \pm v)p$	$(m \pm 1)f$	$A_0^2 F_m F_v / 4\mu_0$
	$(m \pm v)p \pm kQ$	$(m \pm 1)f$	$A_0 A_k F_m F_v / 4\mu_0$
	$(m \pm v)p \pm 2kQ$	$(m \pm 1)f$	$A_{k1} A_{k2} F_m F_v / 16\mu_0$

The vibration displacement Y_m induced by different orders of radial force can be described as

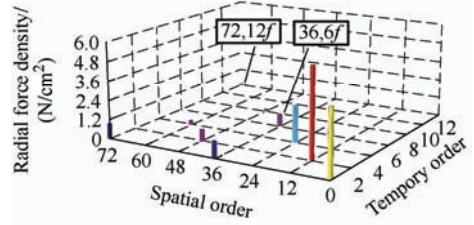
$$Y_m = \begin{cases} \frac{R_y R_s \cdot F_{m=0}}{E \cdot T_y} & m = 0 \\ \frac{12 R_y^3 R_s \cdot F_{m \geq 2}}{E \cdot T_y^3 (m^2 - 1)^2} & m \geq 2 \end{cases} \quad (5)$$

where R_y is the average radius of the stator yoke, R_s is the stator inner diameter, E is the Young's modulus, T_y is the thickness of the stator yoke, and F is the m^{th} -order radial force amplitude. Y_m is a linear variable with F . When $m \geq 2$, Y_m is approximately and inversely proportional to the fourth power of m . $Y_{m=0}/Y_{m \geq 2}$ increases with m , reflecting a more significant zeroth-order deformation for a more prominent m .

Based on Tab. 2 and Eq. (5), increasing the third-harmonic amplitude of the PM magnetic field can deteriorate the zeroth-order vibration in a 36-slot/12-pole SPM machine. Fig. 8a shows the simulated vibration acceleration of this machine, with its peak value emerging at $6f$ and $12f$, which proves its main vibration sources at these two frequencies. A 2D fast Fourier transformation (FFT) of the radial force for the initial machine was performed, and the results are shown in Fig. 8b. The magnitudes of the 36^{th} -order radial force at $6f$ and the 72^{th} -order radial force at $12f$ were the largest. Consequently, the $(36,6f)^{\text{th}}$ and $(72,12f)^{\text{th}}$ radial forces were the main sources of the zeroth-order vibration of this machine, and its vibration response could be improved by decreasing the amplitudes.



(a) Vibration acceleration



(b) 2D FFT decomposition of radial force density

Fig. 8 Finite-element results of vibration acceleration and radial force density of the initial machine

3 Optimization and performance evaluation

The RSM was applied to construct a substitute model for the machine. Moreover, to eliminate the impact of the subjective factors such as the weight coefficients, the BB-MOPSO algorithm was employed to solve the optimization problem. The workflow chart is shown in Fig. 9.

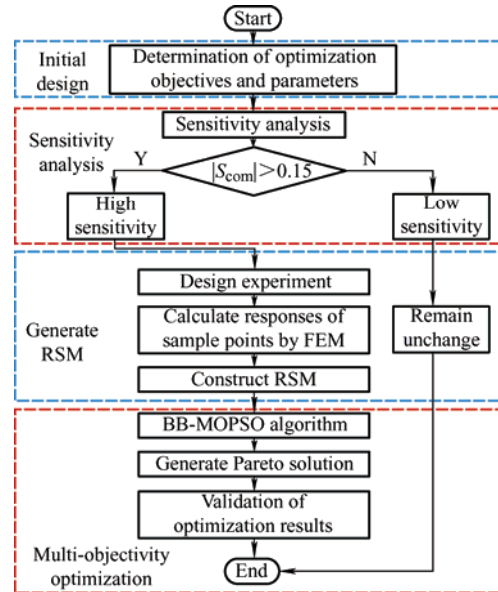


Fig. 9 Complete process of multi-objective optimization

3.1 Sensitivity analysis

The effect of the third-harmonic amplitude of the PM magnetic field on the torque and vibration performance was contradictory in integral-slot SPM machines. Moreover, the sources of the zeroth-order

vibrations were the (36, 6f)th and (72, 12f)th radial forces. Consequently, to obtain the optimal torque and vibration performance, the average torque, torque ripple, (36, 6f)th radial force, and (72, 12f)th radial force were considered as optimization objectives. Eight parameters were selected as optimization variables, such as B_{s0} , as listed in Tab. 3.

Tab. 3 Initial sizes and ranges of variation for design variables

Parameter	Initial	Ranges
Slot-open width B_{s0} /mm	2	1.5-2.5
Slot-wedge width B_{s1} /mm	3.5	3-4
Slot-open height H_{s0} /mm	0.8	0.4-1.2
Slot-wedge height H_{s1} /mm	0.4	0.2-0.8
Slot-body height H_{s2} /mm	13.2	12-15
Fundamental amplitude b_1	1.8	1.4-2.0
Third harmonic amplitude b_3	0.3	0.2-0.4
Compensate coefficient μ	0.2	0.1-0.4

The sensitivity of the design variables is defined as

$$S = \frac{V(E(y|x_n))}{V(y)} \quad (6)$$

where y denotes the optimization objective, $E(y|x_n)$ indicates the average value of y with constant x , and $V(E(y|x_n))$ and $V(y)$ are the variances of $E(y|x_n)$ and y , respectively.

These eight variables were captured using a definitive screening design to generate 17 samples, which substantially reduced the computational cost of the sensitivity analysis. This approach can capture the non-linearity of these variables, while avoiding their coupling effects. However, each variable exhibited a distinct degree of influence on different objectives. Consequently, comprehensive sensitivity was employed to assess the significance of each variable, which can be defined as

$$S_{com}(x_n) = \sum_{k=1,2,3,4} \lambda_k |S_n(x_n)| \quad (7)$$

$$\sum_{k=1,2,3,4} \lambda_k = 1 \quad (8)$$

where λ_k is the weight of the k^{th} optimization target. In this work, $\lambda_1 = \lambda_2 = \lambda_3 = \lambda_4 = 0.25$ was designed to reduce the influence of subjective factors.

Based on Eqs. (6)-(8), the results of the sensitivity calculations are summarized in Tab. 4. To visually distinguish the sensitivities of the different variables, these data are shown in Fig. 10. It is apparent that the

fundamental harmonic, third harmonic, and compensation coefficients exhibited a slightly higher sensitivity than the others variable. Therefore, these variables were selected as the optimization variables for multi-objective optimization.

Tab. 4 Sensitivities of design variables

Parameters	$S_{T_{avg}}(n)$	$S_{T_r}(n)$	$S_{F_r(36,6f)}(n)$	$S_{F_r(72,12f)}(n)$	$S_{com}(n)$
B_{s0}	0.12	0.18	0.08	0.00	0.10
B_{s1}	0.03	0.16	0.06	0.03	0.07
H_{s0}	0.03	0.05	0.03	0.05	0.04
H_{s1}	0.04	0.05	0.03	0.06	0.04
H_{s2}	0.06	0.13	0.23	0.00	0.11
b_1	0.11	0.12	0.22	0.32	0.19
b_3	0.43	0.36	0.54	0.14	0.37
μ	0.30	0.05	0.10	0.28	0.18

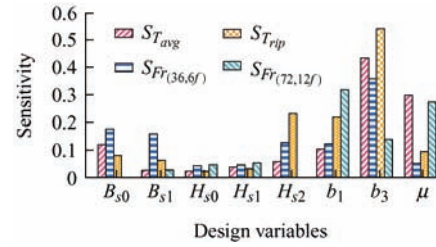


Fig. 10 Sensitivity with different optimization objectives

3.2 Mathematical models based on RSM

In this study, the RSM was used to construct an alternative model to further reduce the computational burden. The Box-Behnken design is a classical method used to establish an RSM. The sample point distribution of the Box-Behnken design with three design variables is shown in Fig. 11. The simulation results were analyzed, and the corresponding polynomial regression model can be expressed as

$$\rho = a_0 + \sum_{i=1}^n a_i \chi_i + \sum_{i=1}^n a_{ii} \chi_i^2 + \sum_{i=1}^n \sum_{j \geq 1} a_{ij} \chi_i \chi_j + \varepsilon \quad (9)$$

where χ_i is the i^{th} of n variables; χ , a_0 , a_i , and a_j are the regression coefficients; and ε is the random error.

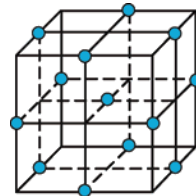


Fig. 11 Samples distribution of Box-Behnken design with three design variables

The RSM fitting accuracy is essential to obtain reliable optimization results. The determination

coefficient R^2 is typically used to assess the fitting accuracy of the RSM, and is defined as

$$R^2 = 1 - \frac{\sum_{i=1}^{\beta} (\rho_i - \hat{\rho}_i)^2}{\sum_{i=1}^{\beta} (\rho_i - \bar{\rho}_i)^2} \quad (10)$$

where β is the number of samples, ρ_i is the response value, $\hat{\rho}_i$ is the estimated value, and $\bar{\rho}_i$ is the average value of the responses.

Fig. 12 shows the partial RSM of the fundamental harmonic, third harmonic, and compensation coefficients. The determination coefficients of all RSM were larger than 0.9, indicating that the fitting accuracy satisfied the requirement and had a high reliability. According to the RSM, the regression equations for the average torque T_{avg} , torque ripple T_{rip} , $(36,6f)^{th}$ radial force, and $(72,12f)^{th}$ radial force were fitted using Eqs. (11)-(14). Because various variables were nonlinearly associated with the objectives, identifying the optimal values through subjective judgment was difficult. Therefore, a compromise design using a multi-objective optimization algorithm was used.

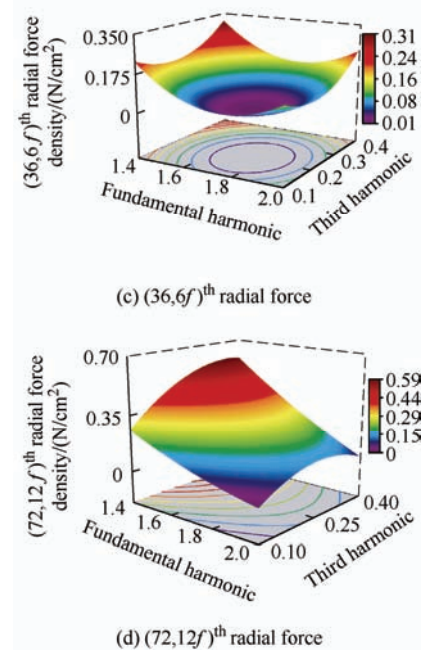
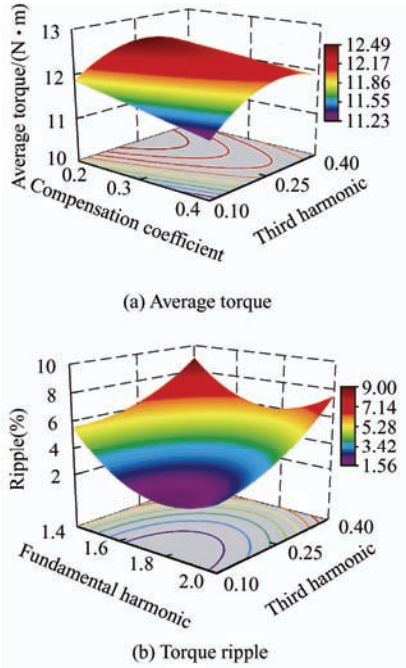


Fig. 12 Response surface on b_1 , b_3 , and μ

$$T_{avg} = 12.16 + 0.47b_1 + 2.44b_3 - 0.23\mu + 4.72b_1b_3 - 1.89b_1\mu + 5.15b_3\mu - 0.47b_1^2 - 20.91b_3^2 - 0.21\mu^2 \quad (11)$$

$$T_{rip} = 173.25 - 131.37b_1 - 35.72b_3 - 345.86\mu + 8.53b_1b_3 + 133.47b_1\mu + 44.83b_3\mu + 25.15b_1^2 + 43.49b_3^2 + 169.49\mu^2 \quad (12)$$

$$F_{r_{(36,6f)}} = 7.90 - 6.28b_1 - 1.84b_3 - 14.36\mu + 0.07b_1b_3 + 5.18b_1\mu + 0.47b_3\mu + 1.34b_1^2 + 3.75b_3^2 + 8.32\mu^2 \quad (13)$$

$$F_{r_{(72,12f)}} = 0.271 - 0.183b_1 + 0.707b_3 - 0.674\mu - 0.148b_1b_3 + 0.167b_1\mu - 0.543b_3\mu + 0.031b_1^2 - 0.460b_3^2 + 0.588\mu^2 \quad (14)$$

3.3 Optimization based on BB-MOPSO

The BB-MOPSO algorithm is based on a particle-updating strategy in which no control parameters need to be adjusted. It employed a time-varying mutation operator to expand its search capability^[30]. The particle update formula is defined as follows

$$P_{m,n}(x+1) = \begin{cases} N\left(\frac{kLi_{m,n}(x) + (1-k)Lg_{m,n}(t)}{2}, |Li_{m,n}(t) - Lg_{m,n}(x)|\right) & U(0,1) < 0.5 \\ Lg_{m,n}(x) & U(0,1) \geq 0.5 \end{cases} \quad (15)$$

where k is an arbitrary number within $[0,1]$, $Li_{m,n}(x)$

and $Lg_{m,n}(x)$ indicate the individual and global optimal

locations, respectively.

Therefore, the BB-MOPSO algorithm was combined with the RSM to quickly optimize the above

$$\left\{ \begin{array}{l} \text{Functions: } f_{\min} = -\beta_1 T_{\text{avg}} + \beta_2 T_{\text{rip}} + \beta_3 F_{r_{(36,6f)}} + \beta_4 F_{r_{(72,12f)}} \\ \text{Constraints: } T_{\text{avg}} \geq 11 \text{ N} \cdot \text{m}, T_{\text{rip}} \leq 13 \\ \quad F_{r_{(36,6f)}} \leq 0.5 \text{ N/cm}^2, F_{r_{(72,12f)}} \leq 0.4 \text{ N/cm}^2 \\ \text{Variables: } b_1, b_3, \mu \end{array} \right. \quad (16)$$

where β_1 , β_2 , β_3 , and β_4 are the weight coefficients of the average torque T_{avg} , torque ripple T_{rip} , $(36,6f)^{\text{th}}$ radial force, and $(72,12f)^{\text{th}}$ radial force, respectively. To balance the machine performance, β_1 , β_2 , β_3 , and β_4 are given as 0.25.

Fig. 13 shows the Pareto front with respect to the average torque, torque ripple, and $(36,6f)^{\text{th}}$ radial force. A contradiction between the objectives is evident. The optimal trade-off solution is marked by black, considering the machine performance requirements comprehensively from the Pareto solutions. The machine performance of sine shaping with an optimal third harmonic was substantially improved compared with that of the initial machine.

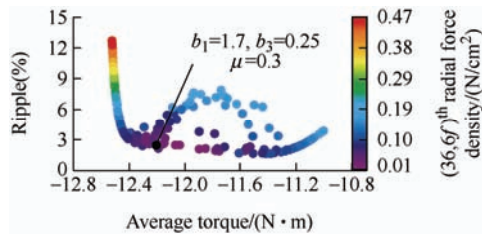


Fig. 13 Pareto optimal solutions of BB-MOPSO algorithm optimization

3.4 Performance evaluation

Fig. 14 compares three different PM shapes, all of which maintain the principle of a constant minimum air gap length. The no-load air-gap flux harmonics and torque performance are shown in Fig. 15. The average torque of the Sin+3rd-shaped PM machine was $12.2 \text{ N} \cdot \text{m}$, which was 4.0% higher than the eccentric PM machine with $11.7 \text{ N} \cdot \text{m}$, and the initial machine with $12.6 \text{ N} \cdot \text{m}$ (100%). Meanwhile, the torque ripple of the initial one was 20.7%, and both the optimal and eccentric PM machines was reduced to 2.9% and 2.1%, respectively. In Fig. 2, one machine with an eccentric distance of 12.2 mm provides a comparable average

highly sensitive variables. The multi-objective optimization function and constraints, which must be satisfied, are as follows

torque; however, the torque ripple increases unacceptably to 9.7%. The superior torque performance of the optimal Sin+3rd-shaped PM machine was derived from the fact that its fundamental and third-harmonic levels are higher than those of an eccentric machine.

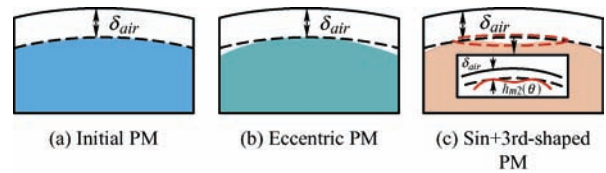


Fig. 14 Comparison of different PM shapes

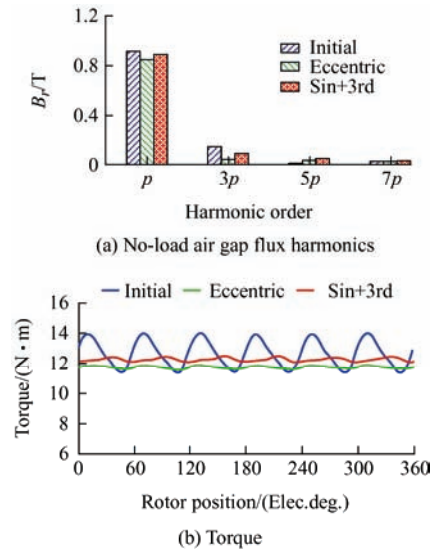


Fig. 15 Comparison of the air-gap magnetic flux and torque waveform

Fig. 16 shows the 2D FFT of the radial force and vibration acceleration of the three machines. The $(36,6f)^{\text{th}}$ and $(72,12f)^{\text{th}}$ radial force amplitudes of machines with eccentric and Sin+3rd-shaped PM decreased, and the vibration performance improved. The vibration acceleration of the third-harmonic-shaped PM machine at $6f$ and $12f$ decreased from 0.15 m/s^2 to 0.006 m/s^2 and 0.006 m/s^2 to 0.003 m/s^2 ,

respectively. The vibration performance of the Sin+3rd-shaped PM machine improved significantly and was almost identical to that of the eccentric machine. Regarding the torque and vibration performance, the Sin+3rd-shaped PM machine was superior and more favorable than the eccentric machine. It was demonstrated that the PM shaping technique with a third harmonic can effectively improve the torque and vibration performance of an integral-slot SPM machine.

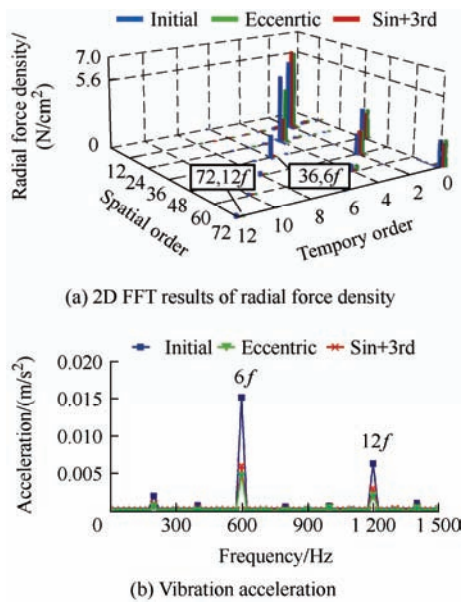


Fig. 16 Comparison of radial force and vibration acceleration

4 Experimental validation

A 36-slot/12-pole integral-slot SPM machine with an eccentric PM was manufactured and tested to verify the theoretical analysis. Fig. 17a presents its prototype. Fig. 17b shows the modal experiments on the stator, stator with coils, and casing. First, a flexible rope was suspended from the stator assembly to simulate unconstrained conditions. Subsequently, several accelerometers were simultaneously installed at different locations on the housing surface to facilitate an accurate acceleration response. The simulation and measurement results of the modal data are summarized in Tab. 5. Because the frequency response measured using the excitation method was limited to 8 kHz, a high modal could not be measured. Thus, the high

modal parameters originated from the simulation results.

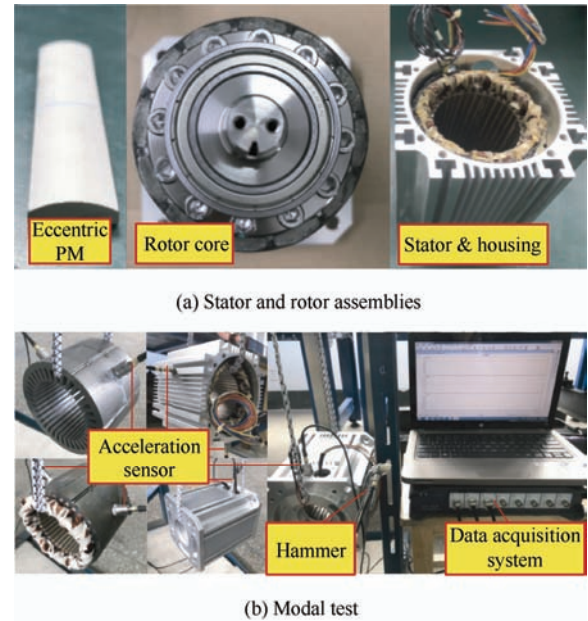


Fig. 17 SPM prototype and modal test

Tab. 5 Modal parameters

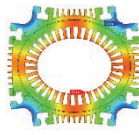


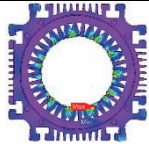
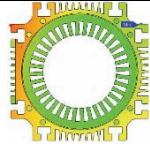
Modal order	2	3	4
Modal shape			
Simulated frequency/Hz	2 250	4 355	6 836
Tested frequency/Hz	2 318	4 450	6 874
Error(%)	3.02	2.19	0.56
Modal order	12	0	
Modal shape			
Simulated frequency/Hz	15 556	17 493	

Fig. 18 shows the experimental platform of the prototype. The simulated and measured no-load back-EMF waveforms at 1 000 r/min are shown in Fig. 19. The measured results agree with the simulated results. Fig. 20a shows the measured three-phase current and torque waveforms at a rated load of 1 000 r/min. The current amplitude was 6.3 A, and the measured average torque was approximately 9.7 N • m with a torque ripple of 4.6%. Fig. 20b shows the simulated and measured vibration accelerations, and

the peaks emerged at $6f$ and $12f$, which is consistent with the simulation and theoretical analysis. The torque performances at different current amplitudes are compared in Fig. 21. The optimal third-harmonic-shaped PM machine displayed superior torque performance. A slight increase in the torque ripple during the experiment was observed, which was attributed to the average torque deficit. A slight difference between the simulation and the measurement was observed, but it was within an acceptable range.

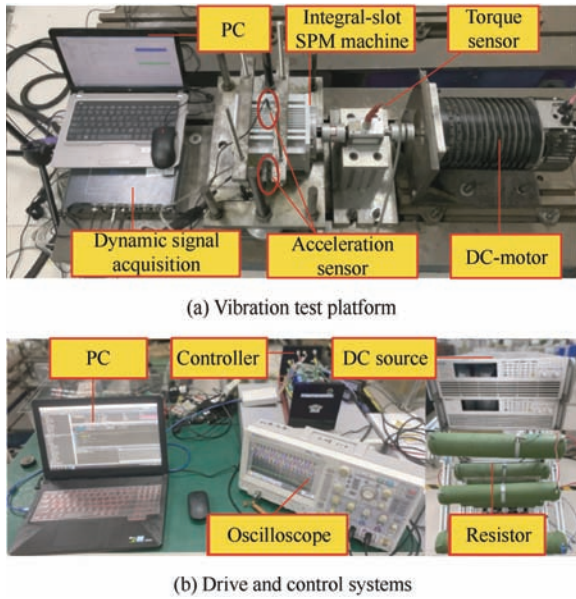


Fig. 18 Test experiment platform

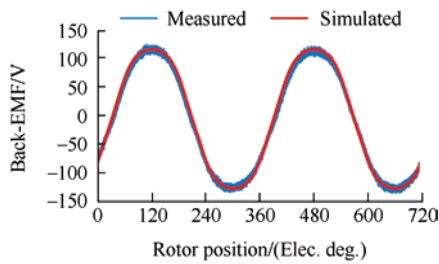
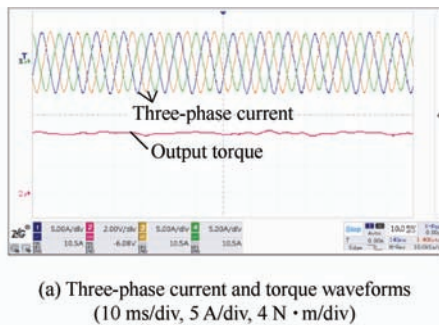


Fig. 19 Comparison of simulated and measured no-load back-EMF at 1000 r/min



(a) Three-phase current and torque waveforms (10 ms/div, 5 A/div, 4 N·m/div)

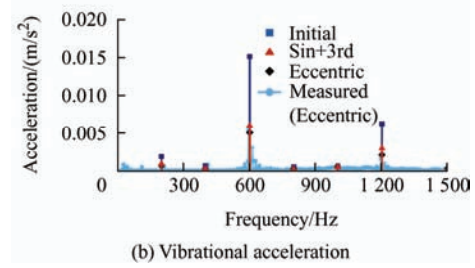


Fig. 20 Comparison of predicted and experimental data at rated load

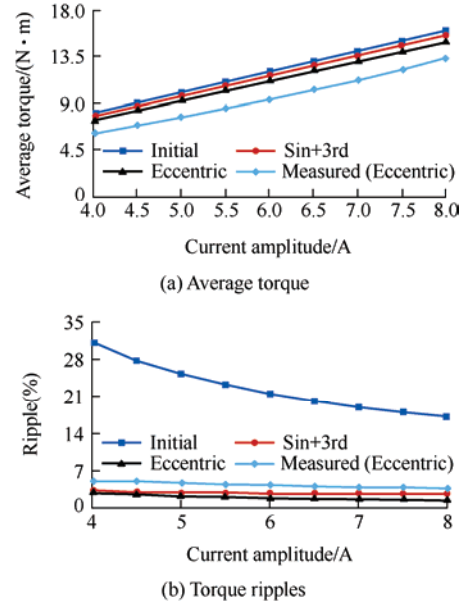


Fig. 21 Comparison of torque performance with different current amplitudes

5 Conclusions

This study investigated a Sin+3rd-shaped PM to improve the vibration and torque performance of an integral-slot SPM machine. First, the effects of the third harmonic of the PM magnetic field on the vibration and torque performance of an integral-slot SPM machine were studied. The Sin+3rd-shaped PM was found to have a contrary effect on the vibration and torque performance. The RSM and BB-MOPSO algorithms were then employed to optimize the harmonic-injected PM shape to improve the vibration and torque performance. The performance advantages of a 36-slot/12-pole SPM machine with an optimal Sin+3rd-shaped PM were verified. The machine was characterized by a high average torque, low torque ripple, and low vibration response. The average torque of the optimal Sin+3rd-shaped PM machine was

enhanced by 4% to 12.2 N • m compared with the eccentric PM machine. The torque ripple was reduced by 10% using an eccentric PM machine with the same torque capability. In addition, the vibration performance was as excellent as that of a machine with an eccentric distance of 16 mm. Finally, an eccentric PM prototype was fabricated and measured, and the results indicate that the experimental and simulation data are in good agreement. Future work will involve the fabrication and testing of a prototype of the Sin+3rd-shaped PM to verify the theoretical analysis. This method is not constrained to the machine used in this study and can be applied to various SPM machines for vibration and torque improvement.

References

- [1] Y Sun, W Zhao, J Ji, et al. Torque improvement in dual m-phase permanent-magnet machines by phase shift for electric ship applications. *IEEE Transactions on Vehicular Technology*, 2020, 69(9): 9601-9612.
- [2] M Slunjski, O Stiscia, M Jones, et al. General torque enhancement approach for a nine-phase surface PMSM with built-in fault tolerance. *IEEE Transactions on Industrial Electronics*, 2021, 68(8): 6412-6423.
- [3] J Ji, Y Zhou, T Tao, et al. Armature MMF reconfiguration method of six-phase integral-slot PMSMs for zero-order vibration reduction under open-circuit faults. *IEEE Transactions on Transportation Electrification*, 2023, doi: 10.1109/TTE.2023.3266612.
- [4] Y Wang, J Ji, W Zhao, et al. Meshless generalized finite difference method to analyze electromagnetic performance of SPM machines with eccentric rotor shape. *IEEE Transactions on Industrial Electronics*, 2022, 69(12): 12055-12065.
- [5] R Dutta, A Pouramin, M F Rahman. A novel rotor topology for high-performance fractional slot concentrated winding interior permanent magnet machine. *IEEE Transactions on Energy Conversion*, 2021, 36(2): 658-670.
- [6] W Zhao, Q He, W Tian, et al. Investigation of winding configuration on electromagnetic vibration in modular dual three-phase PM machine. *IEEE Transactions on Industrial Electronics*, 2023, doi: 10.1109/TIE.2023.3262876.
- [7] F Yan, J Ji, Z Ling, et al. Magnets shifting design of dual PM excited vernier machine for high-torque application. *Chinese Journal of Electrical Engineering*, 2022, 8(3): 90-101.
- [8] J Zhu, Y Zuo, H Chen, et al. Deep-investigated analytical modeling of a surface permanent magnet Vernier motor. *IEEE Transactions on Industrial Electronics*, 2022, 69(12): 12336-12347.
- [9] S Zhu, W Zhao, J Ji, et al. Design to reduce modulated vibration in fractional-slot concentrated-windings PM machines considering slot-pole combination. *IEEE Transactions on Transportation Electrification*, 2023, 9(1): 575-585.
- [10] F Li, K Wang, J Li, et al. Electromagnetic performance analysis of PMSM with eccentric consequent pole rotor. *2017 7th International Conference on Power Electronics Systems and Applications - Smart Mobility, Power Transfer & Security (PESA)*, 12-14 December, 2017, Hong Kong, China. IEEE, 2017: 1-7.
- [11] L Jing, Z H Luo, R H Qu, et al. Investigation of a surface PM machine with segmented-eccentric magnet poles. *IEEE Transactions on Applied Superconductivity*, 2018, 28(3): 1-5.
- [12] T Liu, W Zhao, J Ji, et al. Effects of eccentric magnet on high-frequency vibroacoustic performance in integral-slot SPM machines. *IEEE Transactions on Energy Conversion*, 2021, 36(3): 2393-2403.
- [13] S Zhu, W Zhao, J Ji, et al. Design to reduce electromagnetic vibration in integral-slot SPM machine considering force modulation effect. *Science China Technological Sciences*, 2022, 65(8): 1867-1877.
- [14] K Wang, Z Y Gu, Z Q Zhu, et al. Optimum injected harmonics into magnet shape in multiphase surface-mounted PM machine for maximum output torque. *IEEE Transactions on Industrial Electronics*, 2017, 64(6): 4434-4443.
- [15] K Wang. Effects of harmonics into magnet shape and current of dual three-phase permanent magnet machine on output torque capability. *IEEE Transactions on Industrial Electronics*, 2018, 65(11): 8758-8767.
- [16] G Liu, Y Zeng, W Zhao, et al. Permanent magnet shape

- using analytical feedback function for torque improvement. *IEEE Transactions on Industrial Electronics*, 2018, 65(6): 4619-4630.
- [17] Y Zeng, M Cheng, G Liu, et al. Effects of magnet shape on torque capability of surface-mounted permanent magnet machine for servo applications. *IEEE Transactions on Industrial Electronics*, 2020, 67(4): 2977-2990.
- [18] Y Ma, J Wang, L Zhou, et al. Surrogate-assisted optimization of a five-phase SPM machine with quasi-trapezoidal PMs. *IEEE Transactions on Industrial Electronics*, 2022, 69(1): 202-212.
- [19] M V Alavi, J L Besnerais, A Nysveen. An investigation of zeroth-order radial magnetic forces in low-speed surface-mounted permanent magnet machines. *IEEE Transactions on Magnetics*, 2016, 52(8): 1-6.
- [20] X Li, S Huang, Q Zhang, et al. Electromagnetic noise assessment for EV's PM driving machines. *2014 17th International Conference on Electrical Machines and Systems (ICEMS)*, 22-25 October, 2014, Hangzhou, China. IEEE, 2014: 1552-1555.
- [21] H Fang, D Li, R Qu, et al. Modulation effect of slotted structure on vibration response in electrical machines. *IEEE Transactions on Industrial Electronics*, 2019, 66(4): 2998-3007.
- [22] J Le Besnerais. Vibroacoustic analysis of radial and tangential air-gap magnetic forces in permanent magnet synchronous machines. *IEEE Transactions on Magnetics*, 2015, 51(6): 1-9.
- [23] S Wang, J Hong, Y Sun, et al. Analysis of zeroth-mode slot frequency vibration of integer slot permanent-magnet synchronous motors. *IEEE Transactions on Industrial Electronics*, 2020, 67(4): 2954-2964.
- [24] Y Zhou, J Ji, W Zhao, et al. Modulated vibration reduction design for integral-slot interior permanent magnet synchronous machines. *IEEE Transactions on Industrial Electronics*, 2022, 69(12): 12249-12260.
- [25] D Cao, W Zhao, J Ji, et al. Parametric equivalent magnetic network modeling approach for multiobjective optimization of PM machine. *IEEE Transactions on Industrial Electronics*, 2021, 68(8): 6619-6629.
- [26] X Zhu, M Jiang, Z Xiang, et al. Design and optimization of a flux-modulated permanent magnet motor based on an airgap-harmonic-orientated design methodology. *IEEE Transactions on Industrial Electronics*, 2020, 67(7): 5337-5348.
- [27] J Ji, Y Yang, Z Ling, et al. Multi-objective optimization of interior permanent magnet machine for heavy-duty vehicle direct-drive applications. *IEEE Transactions on Energy Conversion*, 2022, 37(3): 1946-1954.
- [28] S Zuo, F Lin, X Wu. Noise analysis, calculation, and reduction of external rotor permanent-magnet synchronous motor. *IEEE Transactions on Industrial Electronics*, 2015, 62(10): 6204-6212.
- [29] S Zhu, W Zhao, G Liu, et al. Effect of phase shift angle on radial force and vibration behavior in dual three-phase PMSM. *IEEE Transactions on Industrial Electronics*, 2021, 68(4): 2988-2998.
- [30] Y Zhang, D Gong, Z Ding. A bare-bones multi-objective particle swarm optimization algorithm for environmental/economic dispatch. *Information Sciences*, 2012, 192: 213-227.



Jinghua Ji received the B.Sc., M.Sc., and Ph.D. degrees in Electrical Engineering from Jiangsu University, Zhenjiang, China, in 2000, 2003, and 2009, respectively.

Since 2000, she has been with the School of Electrical and Information Engineering, Jiangsu University, where she is currently a Professor. From 2013 to 2014, she was a Visiting Scholar with the Department of Electronic and Electrical Engineering at the University of Sheffield, Sheffield, UK. She has authored and coauthored over 50 technical papers in these areas. Her research interests include electrical machines and motor drives.



Deyou Liu received the B.Sc. degree in Electrical Engineering from Jiangsu University, Zhenjiang, China, in 2020. He is currently working toward the M.Sc. degree in Electrical Engineering at Jiangsu University.

His current research interests include optimized design and analysis of PMSM system.



Yu Zeng received the B.Sc. and M.Sc. degrees in Electrical Engineering from Jiangsu University, Zhenjiang, China, in 2014 and 2017, respectively, and the Ph.D. degree in Electrical Engineering from Southeast University, Nanjing, China, in 2021.

Since 2022, he has been with Jiangsu University, where he is currently a Lecturer with the School of Electrical and Information Engineering. His research interests include the design and analysis of permanent magnet synchronous machines and brushless doubly-fed machines.



Tong Liu received the B.Sc. degree in Electrical Engineering from Jiangsu University, Zhenjiang, China, in 2018. He is currently working toward the Ph. D. degree in Electrical Engineering at Jiangsu University.

His current research interests include modeling and calculation of the electromagnetic force, vibration, and acoustic

noise of PMSM systems.



Wenxiang Zhao (M'08-SM'14) received the B.Sc. and M.Sc. degrees in Electrical Engineering from Jiangsu University, Zhenjiang, China, in 1999 and 2003, respectively, and the Ph.D. degree in Electrical Engineering from Southeast University, Nanjing, China, in 2010.

He has been with Jiangsu University since 2003, where he is currently a Professor with the School of Electrical and Information Engineering. From 2008 to 2009, he was a Research Assistant with the Department of Electrical and Electronic Engineering, University of Hong Kong, Hong Kong, China. From 2013 to 2014, he was a Visiting Professor with the Department of Electronic and Electrical Engineering at the University of Sheffield, Sheffield, UK. He has authored and coauthored over 150 papers published in IEEE Transactions. His current research interests include electric machine design, modeling, fault analysis, and intelligent control.